

GT2010-2' ') \$

NUMERICAL AND EXPERIMENTAL ANALYSIS OF THE EFFECTS OF NON-AXISYMMETRIC CONTOURED STATOR ENDWALLS IN AN AXIAL TURBINE

Thorsten Poehler

Institute of Jet Propulsion and
 Turbomachinery, RWTH Aachen University,
 Templergraben 55,
 52062 Aachen, Germany
 poehler@ist.rwth-aachen.de

Jochen Gier

MTU Aero Engines,
 Dachauer Strasse 665,
 80955 Munich, Germany

Peter Jeschke

Institute of Jet Propulsion and
 Turbomachinery, RWTH Aachen University,
 Templergraben 55,
 52062 Aachen, Germany

ABSTRACT

Numerical and experimental investigations have been performed to determine the effects of non-axisymmetric stator endwall contouring on the efficiency of an axial turbine stage. The influences of the contoured endwalls on the secondary flows in the stator and the rotor have been analyzed by conducting steady and unsteady RANS simulations as well as measurements in the 1.5-stage axial cold air turbine test rig of the Institute of Jet Propulsion and Turbomachinery. Both numerical and experimental results show an aerodynamic improvement of efficiency and secondary kinetic energy through non-axisymmetric endwall contouring. The non-axisymmetric endwall contour induces a vortex, which separates the pressure side leg of the horseshoe vortex from the passage vortex resulting in redistributed and reduced secondary flows. The modified secondary flow pattern increases the torque of the rotor blade in the hub region as a consequence of improved inlet conditions for the rotor as well as a reduction of the time interval the secondary flows are convected through the rotor passage within. Concerning the shroud region the endwall contour had no significant impact on the efficiency as a consequence of a dominating tip clearance vortex system.

NOMENCLATURE

BL	boundary layer
c	velocity
CRV	counter rotating vortex
h	span coordinate, helicity

H	passage height
HSV	horseshoe vortex
l	chord length
np	number of pitchwise measured points per stator 1 pitch
nt	number of time-accurate measured points per rotor blade passage
p	pitch
P	total pressure
Pol	polynomial function
ps	pressure side
PV	passage vortex
r	radius
R	Rotor
skeh	secondary kinetic energy helicity
ss	suction side
SF	secondary flow
S1	stator 1
S2	stator 2
t	timestep in time-accurate measurements
x	axial coordinate

Greek symbols

ζ	phase shift
θ	circumferential coordinate in the measurement grid (integer)
λ_2	criterion for vortex visualizations derived from the second Eigenvalue of the matrix $\mathbf{M} = \mathbf{S}^2 + \mathbf{\Omega}^2$ with S as the shear stress tensor and $\mathbf{\Omega}$ as the vortex tensor
ξ	phase length
ρ	density

σ	weighting function for a radial swirl distribution correction
φ	circumferential coordinate
ω	vorticity

Subscripts

1	first sinusoidal curve
2	second sinusoidal curve
ax	axial
cir	circumferential
fluc	fluctuating
LE	leading edge
pert	perturbation
rad	radial
rel	related to defined dimension
sw	streamwise
TE	trailing edge

Superscripts

~	time averaged
–	mass flow averaged
ˆ	spatially averaged

INTRODUCTION

The demand for an increasing power density in modern turbomachines leads to higher blade loads. The tendency to obtain a reduction of the blade count in order to save production costs and flight weight intensifies this correlation. Higher blade loads cause an increase of three-dimensional flow effects, particularly in regard to secondary flows.

Due to major efforts in research works in the past sixty years, the understanding of the mechanisms of secondary flows has been significantly improved. Sieverding [1] and Langston [2] gave detailed overviews of the mechanism of secondary flows. Based on the knowledge of the sources and development of secondary flows various design concepts have been analyzed to develop advanced turbine blades with minimized intensity and size of secondary flows.

A promising concept was shown by Rose [3], who demonstrated the capability of non-axisymmetric endwall contouring. The basic idea of this design concept is an acceleration of the endwall flow by a concave endwall curvature near the pressure side and a deceleration by a convex endwall curvature at the suction side. This local velocity manipulation reduces the cross-passage pressure gradient, which drives the cross-passage flow and thus the passage vortex.

The research works on the design concept of non-axisymmetric endwalls have been pursued intensely. Comprehensive investigations on this field have been accomplished using the “Durham Cascade“ [4-9]. The transfer of these results to the design of the turbine

blades of a Rolls Royce Trent 500 resulted in an efficiency improvement of 0.4% numerically and 0.59% experimentally [10, 11] for the high pressure turbine and 0.9% for the intermediate pressure turbine [12].

Combinations of non-axisymmetric endwall contouring and three-dimensional blade design have also been investigated, e.g. by Pioske [13], Nagel et al. [14] as well as Nagel and Baier [15]. More recent research works have been conducted by Nguyen and Squires [16], Gustafson et al. [17], Wallin and Eriksson [18], Praisner et al. [19], Knezevici et al. [20], Germain et al. [21], Schuepbach et al. [22] and LaFleur [23].

Although great advances have been achieved, the mechanisms of efficiency improvements by non-axisymmetric contoured endwalls have not been conclusively established yet. In order to make a contribution to this, non-axisymmetric hub and shroud endwalls have been designed by single row 3D CFD simulations coupled with an automatic optimization procedure. The most adequate design has been analyzed by transient CFD simulations as well as time-averaged and time-resolved measurements in a 1.5-stage cold air turbine test rig.

DESIGN SUBJECT

The non-axisymmetric hub and shroud stator endwalls presented in this paper have been designed for the first stator of a 1.5-stage axial flow turbine (represented in fig. 1). The datum blading of the turbine meets state of the art designs, particularly with regard to profiling and load. In order to analyze the effects of the endwall contouring separated from other design concepts, the datum blading does not show any 3D design elements like lean, bow or sweep.

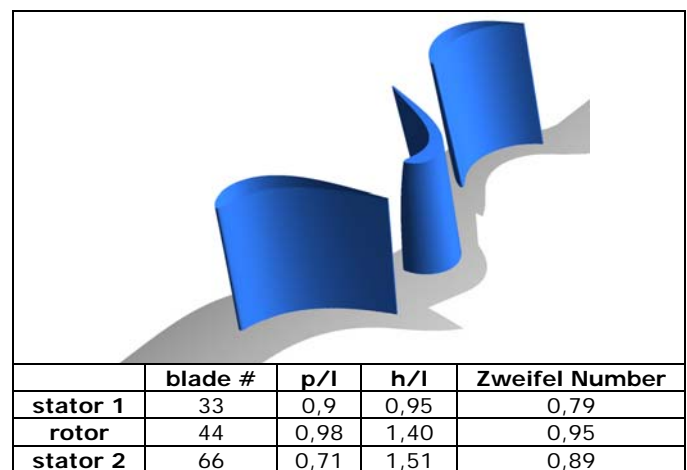


Fig. 1 Blading of the 1.5-stage turbine

Operating at the design conditions, the Reynolds Number of the first stator, based on the exit velocity

and the chord length, is $8.15 \cdot 10^5$. The Exit Mach Number of this aft-load profile is approximately 0.45.

NUMERICAL SIMULATIONS

Numerical Models

The principal tasks of the numerical simulations can be separated into the design of the endwall contouring and the analysis of their effects.

Single row simulations have been performed as a part of an automatic design process in order to generate an adequate endwall contour. During the design process steady state simulations of the 1.5 stages have been conducted in order to validate the conformity of the target function and the stage efficiency. However, to analyze the unsteady effects of the manipulated secondary flows time-resolved results are required, which are also presented in this paper. The solving process is based on a 3D-Reynolds Averaged Navier-Stokes code (Ansys CFX 10.0), applied to structured grids for the spatial discretization. Both steady and unsteady numerical simulations have been conducted using the SST turbulence model and the Low-Reynolds approach for the boundary layer treatment to perform accurate numerical results. For the unsteady simulations the domains have been multiplied (three passages of S1, four passages of R, six passages of S2) to achieve a pitch change of one at the stage-interfaces.

Design optimization

The iteration loop of the automatic optimization process is built by 6 functional units: contouring, pre-processing, solving, post-processing, restaggering (including a rerun of solving and post-processing) and optimizing.

The contouring process uses a method, which directly moves the nodes of the datum hexahedra mesh. The absence of a CAD- and a mesh-generation-program ensures the comparability of the numerical meshes resulting in minimized changes of the discretization error. In order to define the shape of the endwall contour, an orthogonalization is applied to the endwall between the blades (fig. 2). Two polynomial functions of 7th degree define the displacements of the endwall on the suction side and the pressure side. The polynomial functions are connected by sinusoidal curves in circumferential direction.

The arguments of the polynomial functions are set to $x_{rel} = 0, 0.2, 0.4, 0.7, 0.9$ and 1, with

$$x_{rel} = \frac{x - x_{LE}}{x_{TE} - x_{LE}}.$$

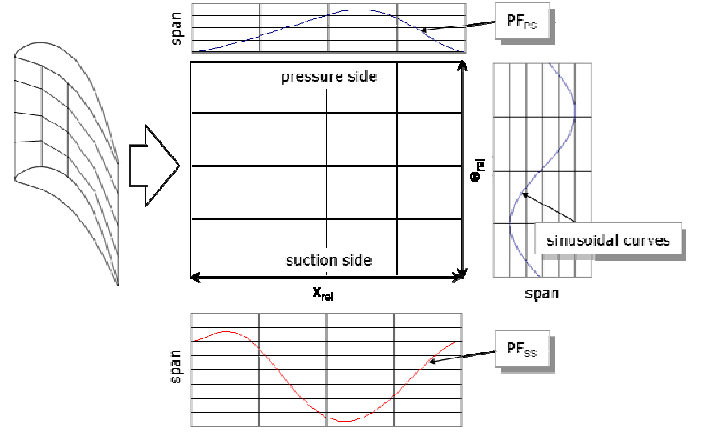


Fig. 2 Principal method of endwall shape geometry definition

In order to ensure a continuous transition between the contoured endwall and the endwall before and behind the blade passage, the displacement and the gradient of both polynomial functions has been set to zero at the leading and the trailing edge:

$$\text{Pol}(x_{rel} = 0) = \text{Pol}(x_{rel} = 1) = 0$$

$$\left. \frac{d\text{Pol}}{dx_{rel}} \right|_{x_{rel}=0} = \left. \frac{d\text{Pol}}{dx_{rel}} \right|_{x_{rel}=1} = 0$$

The polynomial functions are implemented in a linear blending function

$$A = \theta_{rel} \cdot \text{Pol}_{DS} + (1 - \theta_{rel}) \cdot \text{Pol}_{SS},$$

with

$$\theta_{rel} = \frac{\theta - \theta_{SS}}{\theta_{DS} - \theta_{SS}}.$$

This function defines the amplitude of the sinusoidal curves. The local radial displacement of a node of the numerical grid at the endwall is then derived by

$$\Delta r = A \cdot (\sin(\xi_1 \cdot \theta_{rel} + \zeta_1) + \sin(\xi_2 \cdot \theta_{rel} + \zeta_2)).$$

For the iterative improvement of the design, a well-established Sequential Quadratic Programming method has been chosen. The minimum of the secondary kinetic energy weighted by the helicity (skch) was the optimization target, while the capacity

of the blade has been kept constant by means of restaggering of the blade.

Examining the skeh in the stator exit plane gives a quantity, which correlates to the mixing losses expected downstream of the plane. In publications about the analysis of secondary flows and means to their reduction the secondary flow is nearly uniformly defined as the deviation of the flow from a primary flow. However, a common agreement of an adequate definition of the primary flow has not been achieved. Since the success of the optimization depends on the accuracy of the examination of the secondary flow, the precise definition of the primary flow is of crucial importance. In order to obviate a misdirection of the optimizing process, the primary flow has to be defined as a flow, which can technically be provided by means of a geometrical design. The mean exit flow angle of the primary flow has to meet the one of the real flow and should comprise the endwall boundary layers and the wake. In this paper, the primary flow was examined by a mass flow weighted averaging of the velocity components of the real flow in the stator exit plane:

$$\tilde{c}_{ax} = \frac{\int \rho \cdot c_{ax}^2 \cdot \Delta\varphi \cdot r \, dr}{\int \rho \cdot c_{ax} \cdot \Delta\varphi \cdot r \, dr}$$

$$\tilde{c}_{rad} = \frac{\int \rho \cdot c_{rad} \cdot c_{ax} \cdot \Delta\varphi \cdot r \, dr}{\int \rho \cdot c_{ax} \cdot \Delta\varphi \cdot r \, dr}$$

$$\tilde{c}_{cir} = \sigma(r) \cdot \frac{\int \rho \cdot c_{cir} \cdot c_{ax} \cdot \Delta r \cdot r \, d\varphi}{\int \rho \cdot c_{ax} \cdot \Delta r \cdot r \, d\varphi}$$

The intention of the circumferential and the radial averaging is to even out the components of the secondary flow vortices. In the circumferential direction, the additional function $\sigma(r)$ ensures the same radial swirl distribution as intended initially in the design of the datum blading, i.e. without the effects of secondary flows. Thus the correct radial distribution of the pitchwise exit flow angle is provided by the primary flow.

The kinetic energy of the secondary flow is then derived from

$$ske = \frac{1}{2} c_{sek}^2 = \frac{1}{2} (c^2 - \tilde{c}^2).$$

leading to the skeh:

$$skeh = ske \cdot h = \frac{1}{2} c_{sek}^2 \cdot \frac{\bar{\omega} \cdot \bar{c}}{|\bar{\omega}| \cdot |\bar{c}|}.$$

EXPERIMENTAL SETUP

Axial turbine test rig

The experiments have been conducted at the axial cold air turbine test rig (represented in fig. 3) of the Institute of Jet Propulsion and Turbomachinery of the RWTH Aachen University.

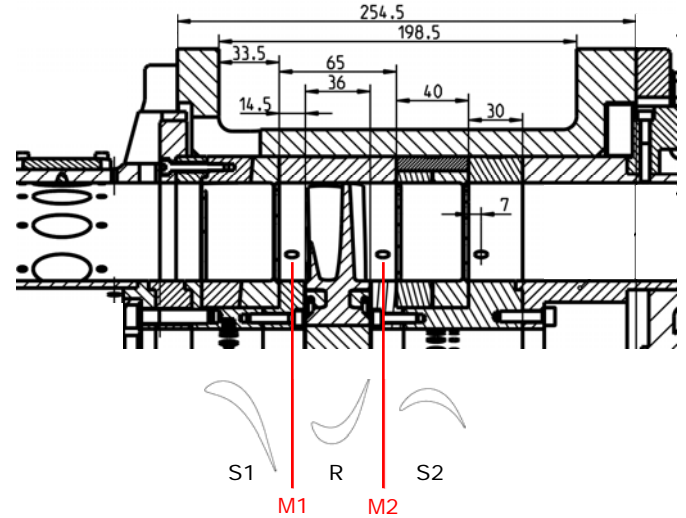


Fig. 3 Axial cold air turbine test rig

The test rig features an automatic operating point regulation ensuring stable inlet and outlet pressure levels as well as a constant engine speed of 3500 rpm (max. deviation < 0.15%). The mass flow rate in the design point is about 8.5 kg/s with an uncertainty of 0.15%. Additional information specifying the type of the machine is given in table 1.

expansion ratio	enthalpy's degree of reaction	enthalpy parameter	flow coefficient
1.3	0.491	2.056	0.574

Table 1 Turbine-specific parameter and coefficients

Experimental data acquisition

The air turbine possesses probe accesses in several measurement planes (fig. 3). In the planes M1 and M2 the data acquisition was conducted in a measurement grid of high spatial resolution (fig. 4). The circumferential direction was resolved with 23 points and a step size of equidistant 0.5 degree. This corresponds to about 4.583% of the largest pitch (stator 1). In radial direction the spatial resolution of 41 points was refined towards the endwalls. The step size amounts to 3.6364% of the passage height within the mid passage. Near the endwalls the step size was reduced to 1.8182% of the passage height. In order to resolve the flow pattern of the stronger secondary flows at the shroud in M1 and the tip clearance vortex

in M2 accurately, the region of higher spatial resolution was extended in the upper part of the measurement grid.

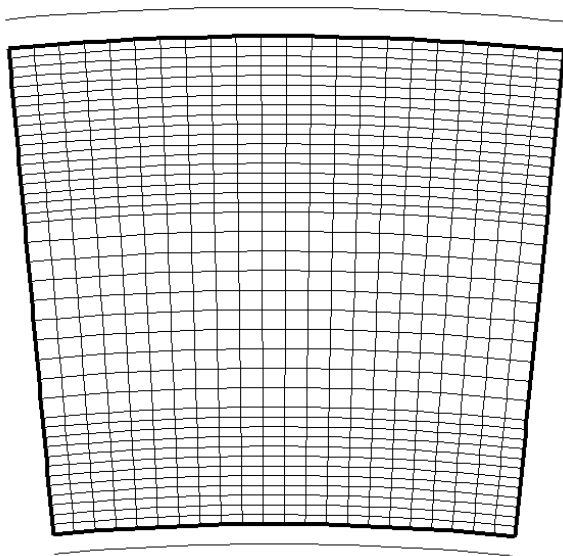


Fig. 4 Measurement grid

Steady measurements have been conducted by using a five hole probe equipped with a thermo couple sensor for temperature measurements. The diameter of the probe head is 2.5mm, which is the circumferential step size in the measurement grid at approximately 75.4% of the passage height. In order to evaluate the isentropic efficiency, measurements of total pressure and total temperature have been evaluated in the settling chamber upstream with chronological synchronism to the five hole probe measurements. The uncertainty of the circumferential averaged isentropic efficiency is about 0.566%.

For the time-resolved measurements of the total pressure a probe with a single pressure transducer has been used. The calibration of this probe has shown an independency of the total pressure measurement in a range of $\pm 15^\circ$ of the flow angle. For each point of the measurement grid 256 samples with an ensemble-averaging of 232 blocks have been recorded.

NUMERICAL AND EXPERIMENTAL RESULTS

Shapes of the contoured endwalls

The shape of the non-axisymmetric endwall contour is presented in fig. 5. The combination of two sinusoidal curves in circumferential direction results in a wavy shape of the endwall.

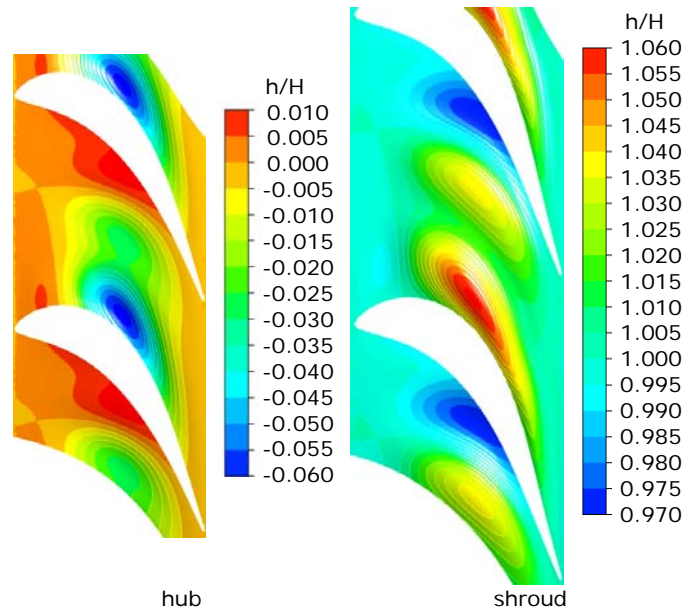


Fig. 5 Contoured endwalls

Results Stator 1

The numerical results of the optimization process for the shroud contour are represented in fig. 6. As the effects of the contour are nearly the same for hub and shroud, only the results of the shroud contour are presented and described in this paper. In order to visualize the vortices as well as skewed boundary layers, streamwise vorticity ω_{sw} has been chosen as the visualization criterion. The contour plots have been examined on surfaces of constant axial coordinate b with an axial direction of view:

$x_{rel} = 0.5$: Contour plots of streamwise vorticity at 50 percent of the axial chord length are shown in the first row of fig. 6. The pressure side leg of the horseshoe vortex is approximately of the same size but reduced intensity in the contoured case. Of course, care has to be taken concerning discussions on the size of a vortex as it depends on its orientation to the surface of visualizations. However, the radial extensions of the vortices are of the same size. The well-known effect of reduced cross-passage flow in case of contoured endwalls decreases the accretion of the pressure side leg of the horseshoe vortex. The suction side of the horseshoe vortex has been spatially increased but reduced concerning its intensity, which is a general effect of the deceleration of the flow in regions of convex curvature at the contoured endwall in combination with the constant swirl of the vortex. Additionally a skewed boundary layer can be found in this contour plot, which is the source of the passage vortex. It appears to be larger in the contoured case. This is a result of the increased static pressure in the convex curvature of the contour. The incoming

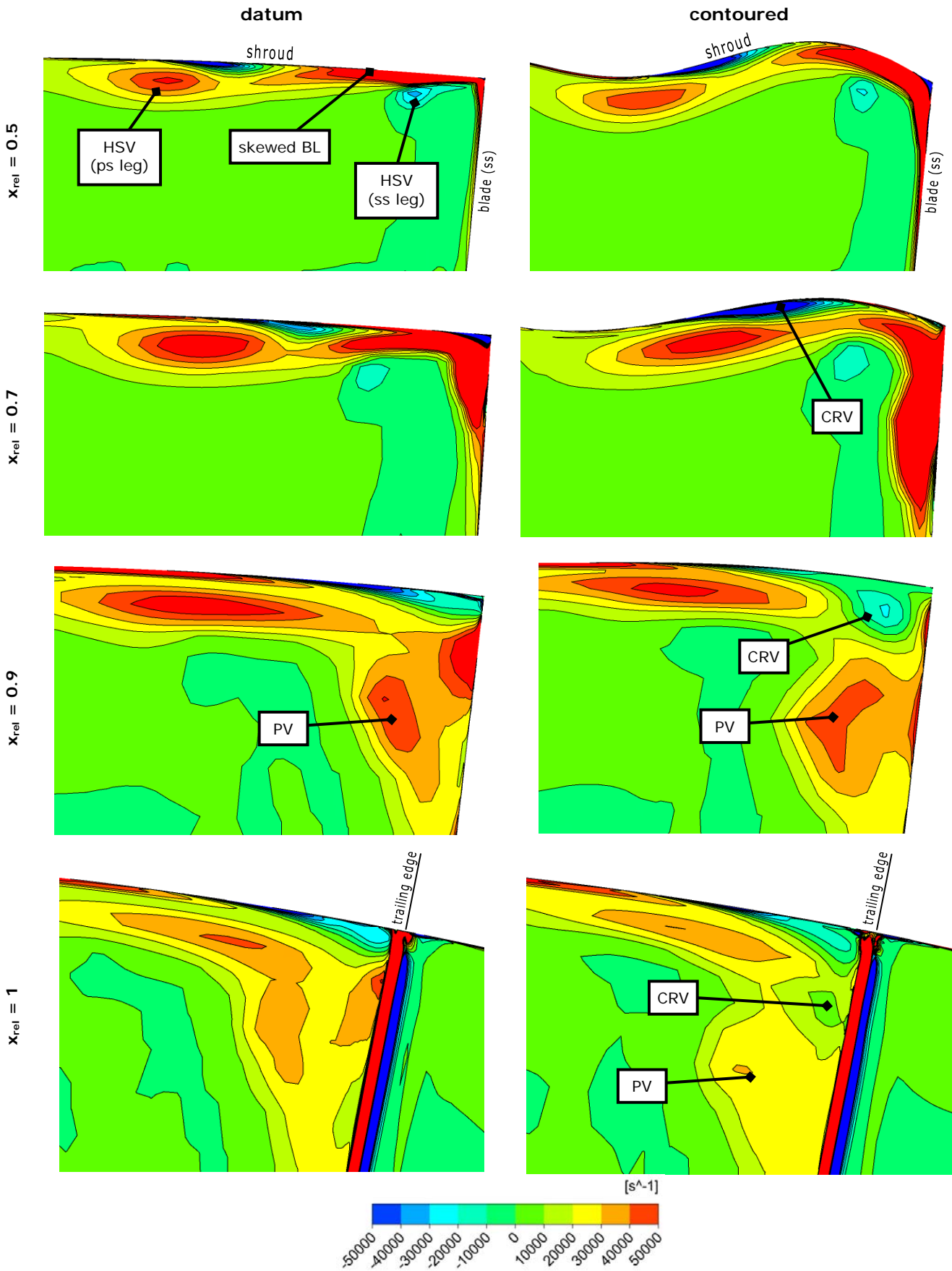


Fig. 6 Streamwise vorticity in the stator passage

boundary layer flow is inclined to avoid this region by turning towards the blade. Additionally, this flow is supported by the radial static pressure gradient resulting from the general deflection of the flow in the stator. The centripetal pressure gradient drives a “cross-blade flow” in centripetal direction analogues to the cross-passage pressure gradient, which drives the cross-passage flow. At this point, of course a distinction has to be made to the hub contour, because the centripetal pressure gradient supports the passage vortex generation at the shroud side while it restrains the passage vortex generation at the hub side.

$x_{rel} = 0.7$: At 70 percent of the axial chord length the passage vortex generation process appears to be in progress in the planar case, while it is nearly finished in the contoured case. The pressure side leg of the horseshoe vortex induces a counter rotating vortex in the boundary layer. The counter rotating vortex is much stronger at the contoured endwall with respect to intensity and size.

$x_{rel} = 0.9$: The counter rotating vortex has been convected to the corner of the contoured endwall. It keeps the pressure side leg of the horseshoe vortex away from the profile. This can also be concluded from the spatial extension of the pressure side leg of the horseshoe vortex in this plot which is a result of the stronger axial component of the orientation of the vortex. The cavity of the non-axisymmetric endwall has been shifted to the radial level of the datum endwall. This shape induces an acceleration of the flow in the cavity. This locally reduces the radial pressure gradient resulting in a decreasing cross-blade flow. The suction side leg of the horseshoe vortex has been dissipated in both cases.

$x_{rel} = 1$: The counter rotating vortex has successfully separated the pressure side leg from the horseshoe vortex in the contoured case. This results in a decreased secondary kinetic energy. In case of the planar endwall the vortices are intermingled, according to the majority of classical secondary flow models.

The radial distribution of total pressure loss as well as their overall values examined in the stator exit plane (M1) is demonstrated in fig. 7. The comparison of the experimental and numerical results shows, that the CFD method has not predicted the level of the total pressure loss very well. In the experimental results a reduction of the profile loss of approximately 10% can be detected. This effect of the endwall contour has already been found by Germain et al. [21]. The reduced profile loss

presented there has not been predicted by the CFD-Code, analogous to the results shown here. The increased aft-load of the profile induced by the potential field of the contoured endwalls seems to affect the whole flow around a blade with a low aspect ratio. Concerning the secondary flow losses both numerical and experimental results show a loss improvement on both endwalls as a result of the modified secondary flow pattern. The experimental results show, that the loss cores in the upper part of the passage are radially distributed, while they are superposed at 70% of the passage height in the CFD results. However, the loss reduction of -0.005 in the CFD results approximately meets the one of the experiments (-0.008), especially if the reduced profile loss is taken into account.

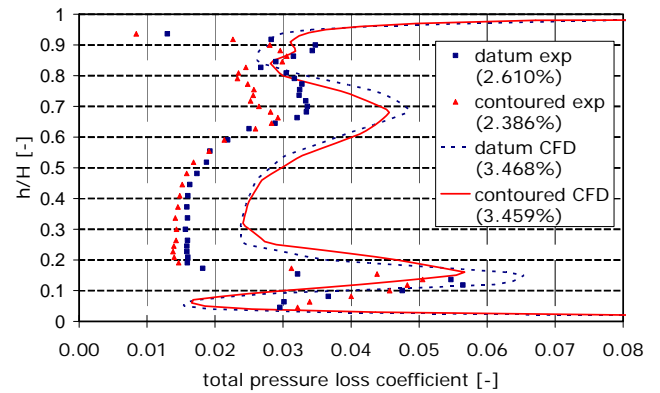


Fig. 7 Total pressure loss in M1

Results Rotor

Time-resolved total pressure measurements have been conducted in the rotor exit plane. All values presented here are ensemble-averaged. The RMS values of the total pressure time-fluctuation can be determined as follows:

$$\bar{P}_{fluc}(r, \Theta) = \sqrt{\frac{1}{nt} \sum_{t=t_0}^{nt-t_0} (P(t, r, \Theta) - \bar{P}(r, \Theta))^2}$$

with

$$\bar{P}(r, \Theta) = \frac{1}{nt} \sum_{t=t_0}^{nt-t_0} P(t, r, \Theta)$$

Examining the RMS values of the circumferential fluctuation of \bar{P}_{fluc} gives a spatially resolved quantity representing total pressure perturbations induced by wakes and secondary flows from the upstream stator and the potential field of the downstream stator:

$$\hat{P}_{\text{pert}}(\mathbf{r}) = \sqrt{\frac{1}{np} \sum_{\Theta=0}^{np} (\bar{P}_{\text{fluc}}(\mathbf{r}, \Theta) - \hat{P}_{\text{fluc}}(\mathbf{r}))^2}$$

with

$$\hat{P}_{\text{fluc}}(\mathbf{r}) = \frac{1}{np} \sum_{\Theta=0}^{np} (\bar{P}_{\text{fluc}}(\mathbf{r}, \Theta))$$

The radial distribution of the values of \hat{P}_{pert} is shown in fig. 8. The region, which is dominated by the tip clearance vortex system ($h/H > 0.6$) as well as the free stream ($0.2 < h/H < 0.6$), shows a reduction of total pressure fluctuations in the contoured case.

The tip clearance vortex system is spatially decreased slightly. In the hub region approximately no improvement can be detected. In comparison to fig. 9, which shows the radial distribution as well as the overall values of the isentropic efficiency, it can be asserted, that regarding the tip clearance vortex system the reduced total pressure fluctuations as well as the reduced total pressure loss of the contoured stator approximately have no impact on the efficiency. The secondary flows of stator 1 affect the tip clearance vortex resulting in a reduced pulsation of the tip clearance vortex. However, it is the strength of the vortex, which dominates the efficiency in this region. In contrast to this the reduced pulsation in the main (which is a consequence of the reduced profile loss of the contoured stator) flow increases the work load. Both effects (reduced profile loss and higher work load) result in a higher efficiency.

The hub region ($0.1 < h/H < 0.2$) shows an efficiency improvement, although the pressure fluctuations have been increased by the contour. It has been found, that there are strong secondary flows in this region. The clearance between the hub of stator 1 and the hub of the rotor induces a very strong vortex, which is convected into the rotor passage. Thus the mean loss in this region is very high. The reduced secondary flows of the upstream stator are convected through the rotor passage within a shorter timeframe in the contoured case. Therefore the extended timeframe of higher total pressure (the timeframe, where no secondary flows of the upstream stator pass through the examination plane) results in a higher total pressure perturbation. This effect is also detected in the numerical results. In fig. 10 the torque at the rotor at $h/H < 0.2$ is plotted against the timestep normalized by the timeframe, which a rotor blade needs to pass a full stator 1 pitch. The results have been derived from the unsteady CFD simulations. The development of the torque values is characterized by two turning points at approximately $t/T = 0.1$ (“low point phase”) and $t/T = 0.42$ (high point phase”) as well as a plateau at approximately $t/T = 0.775$

(“plateau phase”). Furthermore, vortices within the hub region of the rotor passage are demonstrated by means of isosurfaces of $\lambda_2 = -2 \cdot 10^6$ for the timesteps $t/T = 0.1$ and $t/T = 0.775$. The sense of rotation is marked by red (positive) and blue (negative) colors.

Concerning the low point phase ($t/T = 0.1$) it can be stated that the timescale of this phase is reduced in the contoured case. Figure 10 shows, that this phase is characterized by the secondary flows of stator 1 affecting the suction side of the rotor blade behind the throat of the rotor. Corresponding to this effect, the phase modification is neutralized in the “plateau phase” around $t/T = 0.775$. At this point in time, the secondary flows of stator 1 affecting the pressure side of the rotor blade have left the rotor passage, as shown in fig. 10. Thus, the timescale of the “plateau phase” is extended in the contoured case. The result of both phase modifications as a consequence of the endwall contouring is an increase of the torque, which leads to an increase of efficiency.

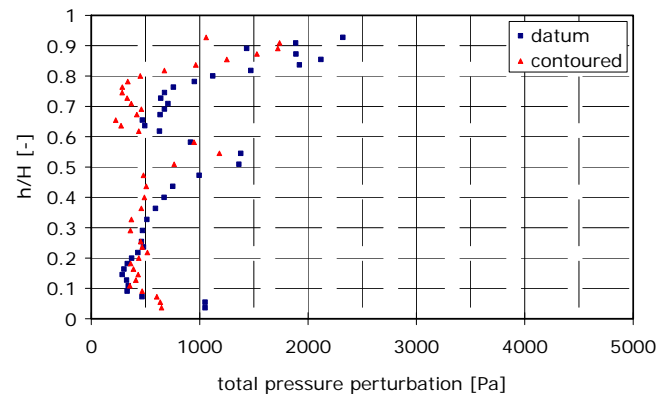


Fig. 8 Total pressure perturbations in the rotor exit plane

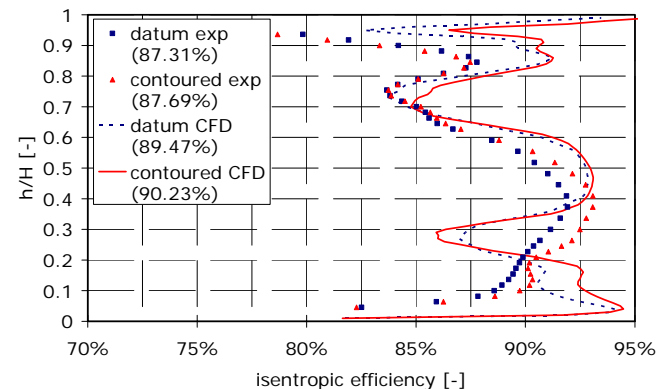


Fig. 9 Isentropic Efficiency of the turbine stage

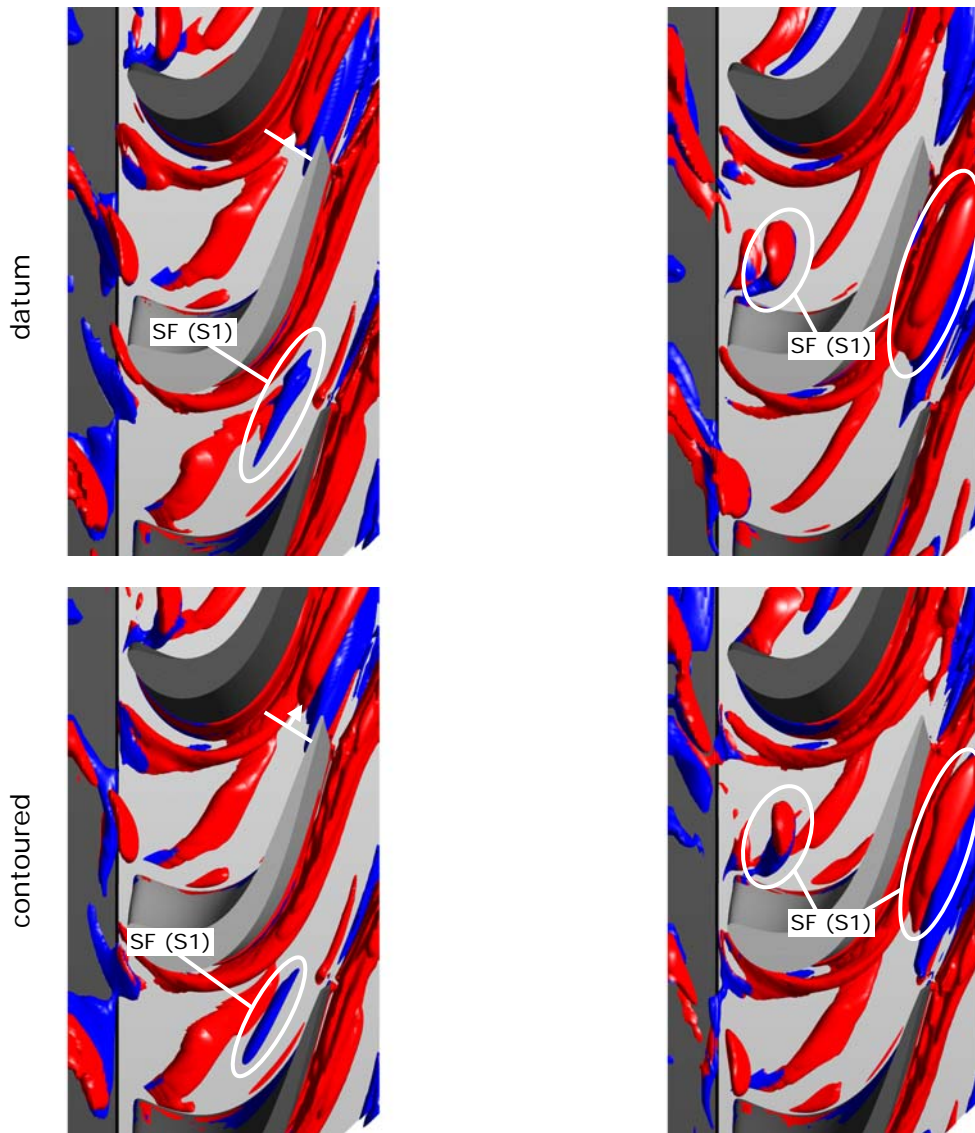
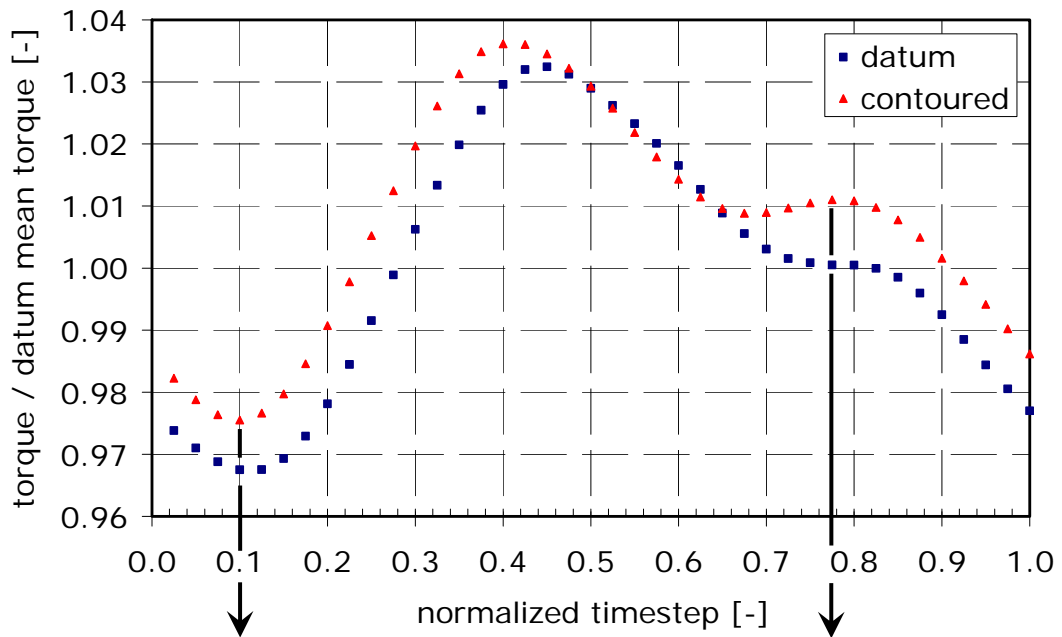


Fig. 10 Rotor hub secondary flows and torque

CONCLUSIONS

The numerical simulations presented in this paper have shown that non-axisymmetric endwall contouring can significantly influence the sources and development of secondary flows. The mechanisms of this impact depend on the datum secondary flow pattern, because the formation of the counter rotating vortex, which separates the pressure side leg of the horseshoe vortex and the passage vortex, depends on the initial behavior of these vortices.

The separation of the secondary flow vortices modifies the total pressure fluctuation at the rotor exit. Concerning the analysis of these fluctuations a distinction has to be made between fluctuations of the secondary flows generated within the rotor, induced by the secondary flows of the upstream stator and fluctuations caused by the secondary flows generated within the upstream stator being convected through the rotor passage. The reduced total pressure fluctuation of the rotor tip clearance vortex system had no significant effect on the stage efficiency. In contrast to this, the modified secondary flows of the upstream stator increased the torque of the rotor by two mechanisms. Improved inlet conditions near the endwall lead to an overall improved performance. Additionally the time-reduced convection of the upstream stator secondary flows diminishes the phase of decreased torque and extends of the phase of higher torque.

Surprisingly the endwall contouring reduced the total pressure loss of the secondary flows in the upper part of the stator passage, but the efficiency in this region has not been improved. Further research work is required to analyse this effect.

ACKNOWLEDGEMENTS

The results presented in this paper are gained from the project "3D-Turbinenstufe". The project was funded by the Forschungsvereinigung für Verbrennungskraftmaschinen (FVV). The authors would like to express their gratitude to the whole Arbeitskreis for their support and the possibility to publish the results.

REFERENCES

- [1] Sieverding C.H., 1984, "Recent Progress in the Understanding of Basic Aspects of Secondary Flows in Turbine Blade Passages", 84-GT-78, ASME 1984, Amsterdam, Netherlands
- [2] Langston, L.S., 2001, "Secondary Flows in Axial Turbines – A Review", Heat and Mass Transfer in Gas Turbine Systems, Vol. 943 of the Annals of the New York Academy of Science
- [3] Rose M.G., 1994, "Non-Axisymmetric Endwall Profiling in the HP NGV's of an Axial Flow Gas Turbine", 94-GT-249, ASME 1994, The Hague, Netherlands
- [4] Harvey N.W., Rose M.G., Taylor M.D., Shahpar S., Hartland J., Gregory-Smith D.G., 1999, "Non-Axisymmetric Turbine End Wall Design, Part I Three-Dimensional Linear Design System", 99-GT-337, ASME 1999, The Hague, Netherlands,
- [5] Ingram G., Gregory-Smith D., Rose M., Harvey N. and Brennan G., 2002, "The Effect of End-Wall Profiling on Secondary Flow and Loss Development in a Turbine Cascade", GT-2002-30339, ASME 2002, Amsterdam, Netherlands
- [6] Hartland J. and Gregory-Smith D., 2002, "A Design Method for the Profiling of End Walls in Turbines", GT-2002-30433, ASME 2002, Amsterdam, Netherlands
- [7] Ingram G., Gregory-Smith D., Rose M., 2003, "Quantification of the Benefits of End-Wall Profiling in a Turbine Cascade", ISABE-2003-1101, ISABE 2003, Cleveland, USA
- [8] Ingram G., Gregory-Smith D., Harvey N., 2004, "Investigation of a Novel Secondary Flow Feature in a Turbine Cascade with End Wall Profiling", GT2004-53589, ASME 2004, Vienna, Austria
- [9] Bagshaw D., Gregory-Smith D., Ingram G. and Stokes M., 2008, "Using Profiled Endwalls, Blade Lean and Leading Edge Extensions to Minimize Secondary Flow", ASME 2008, Berlin, Germany, GT2008-50811
- [10] Brennan G., Harvey N.W., Rose M.G., Fomision N. and Taylor M.D., 2001, "Improving the Efficiency of the Trent 500 HP Turbine using Non-Axisymmetric End Walls, Part 1: Turbine Design", 2001-GT-0444, ASME 2001, New Orleans, USA
- [11] Rose M.G., Harvey N.W., Seaman P., Newman D.A. and McManus D., 2001, "Improving the Efficiency of the Trent 500 HP Turbine using Non-Axisymmetric End Walls, Part 2: Experimental Validation", 2001-GT-0505, ASME 2001, New Orleans, USA
- [12] Harvey N.W., Brennan G., Newman D.A. and Rose M.G., 2002, "Improving Turbine Efficiency using Non-Axisymmetric End Walls, Validation in the Multi-Row Environment and with Low Aspect Ratio Blading", GT-2002-30337, ASME 2002, Amsterdam, Netherlands
- [13] Pioske C., 1998, "3D-Gestaltungskonzepte für Turbinenleiträder unter besonderer Berücksichtigung des Sekundärströmungsverhaltens", PhD Thesis, RWTH Aachen University, Germany
- [14] Nagel M., Fottner L. and Baier R.-D., 2001, "Optimisation of Three Dimensionally Designed Turbine Blades and Side Walls", IS-2001-1058, ISABE 2001, Bangalore, India
- [15] Nagel M. G., Baier R.-D., 2003, "Experimental verified numerical Optimisation of a 3D-parametrised Turbine

- Vane with non-axisymmetric End Walls”, GT2003-38624, ASME 2003, Atlanta, USA
- [16] Nguyen B. Q. and Squires K. D., 2007, “A Simple Procedure to Reduce Secondary Flow Effect in Turbine Nozzle Guide Vanes”, GT2007-28159, ASME 2007, Montreal, Canada,
- [17] Gustafson R., Mahmood G. and Acharya S., 2007, “Aerodynamic Measurements in a Linear Turbine Blade Passage With Three-Dimensional Endwall Contouring”, GT2007-28073, ASME 2007 Montreal, Canada
- [18] Wallin F. and Eriksson L.-E., 2007, “Non-axisymmetric Endwall Shape Optimization of an Intermediate Turbine Duct”, ISABE-2007-1300, ISABE 2007, Beijing, China
- [19] Praisner T. J., Allen-Bradley E., Knezevici D. C., Sjolander S. A., and Grover E. A., 2007, “Application of Non-Axisymmetric Endwall Contouring to Conventional and High-Lift Turbine Airfoils”, GT2007-27579, ASME 2007 Montreal, Canada
- [20] Knezevici D. C., Sjolander S. A., Praisner T. J., Allen-Bradley E. and Grover E. A., 2008, “Measurements of Secondary Losses in a Turbine Cascade With the Implementation of Non-Axisymmetric Endwall Contouring”, GT2008-51311, ASME 2008, Berlin, Germany
- [21] Germain T., Nagel M., Raab I., Schuepbach P., Rose M. and Abhari R. S., 2008, “Improving Efficiency of a High Work Turbine Using Non-Axisymmetric Endwalls, Part I: Endwall Design and Performance”, GT2008-50469, ASME 2008, Berlin, Germany
- [22] Schuepbach P., Rose M., Abhari R. S., Germain T., Raab I. and Gier J., 2008, “Improving Efficiency of a High-Work Turbine Using Non-Axisymmetric Endwalls, Part II: Time Resolved Flow Physics”, GT2008-50470, ASME 2008, Berlin, Germany
- [23] LaFleur R. S., Second Vane Total Pressure Loss Due to Endwall Iceform Contouring, ASME 2008, Berlin, Germany, GT2008-50439